Monthly Notices
of the
ROYAL ASTRONOMICAL SOCIETY
MNRAS **455,** 4388–4398 (2016) doi:10.1093/mnras/stv2644

Clump formation through colliding stellar winds in the Galactic Centre

D. Calderón,[1⋆] A. Ballone,[2,3] J. Cuadra,[1] M. Schartmann,[4] A. Burkert[2,3] and S. Gillessen[2]

[1]*Instituto de Astrofísica, Facultad de Física, Pontificia Universidad Católica de Chile, 782-0436 Santiago, Chile*
[2]*Max Planck Institute for Extraterrestrial Physics, PO Box 1312, Giessenbachstr., D-85741 Garching, Germany*
[3]*Universitätssternwarte der Ludwig-Maximilians-Universität, Scheinerstr. 1, D-81679 München, Germany*
[4]*Centre for Astrophysics and Supercomputing, Swinburne University of Technology, Hawthorn, VIC 3122, Australia*

Accepted 2015 November 9. Received 2015 November 9; in original form 2015 July 21

ABSTRACT

The gas cloud G2 is currently being tidally disrupted by the Galactic Centre supermassive black hole, Sgr A*. The region around the black hole is populated by ∼30 Wolf–Rayet stars, which produce strong outflows. We explore the possibility that gas clumps, such as G2, originate from the collision of stellar winds via the *non-linear thin shell instability*. Following an analytical approach, we study the thermal evolution of slabs formed in the symmetric collision of winds, evaluating whether instabilities occur, and estimating possible clump masses. We find that the collision of relatively slow ($\lesssim$750 km s^{-1}) and strong ($\sim 10^{-5}$ M$_\odot$ yr^{-1}) stellar winds from stars at short separations (<10 mpc) is a process that indeed could produce clumps of G2's mass and above. Such short separation encounters of single stars along their known orbits are not common in the Galactic Centre, making this process a possible but unlikely origin for G2. We also discuss clump formation in close binaries such as IRS 16SW and in asymmetric encounters as promising alternatives that deserve further numerical study.

Key words: hydrodynamics – instabilities – stars: winds, outflows – Galaxy: centre.

1 INTRODUCTION

Gillessen et al. (2012) detected a moving diffuse object, the so-called G2 cloud, on its way towards Sgr A*, the radio source identified as the central massive black hole of our Galaxy (see Genzel, Eisenhauer & Gillessen 2010, for a review). The tidal disruption of this cloud is being monitored by different groups (e.g. Eckart et al. 2013; Gillessen et al. 2013; Phifer et al. 2013) and provides a unique opportunity to test accretion physics, due to both its proximity and the time-scale on which it happens. Gillessen et al. (2012) estimated the mass of G2 to be ∼3 M$_\oplus$ from its line emission. However, the nature of G2 has not been clarified yet. In particular, there is an ongoing debate on whether the diffuse cloud contains a compact mass (likely a star). Witzel et al. (2014) presented the detection of a compact source at 3.8 μm (thermal dust emission) that would correspond to G2 during pericentre passage. Its survival as a compact source to the close passage (∼2000 Schwarzchild radii) suggests the existence of a central star keeping it bound, which they argue is a binary merger product (Prodan, Antonini & Perets 2015). Other possible explanations for a central mass in G2 include an evaporating protoplanetary disc or the wind of a T-Tauri star (Murray-Clay & Loeb 2012; Ballone et al. 2013; Scoville & Burkert 2013; De Colle et al. 2014).

On the other hand, Pfuhl et al. (2015) argued in favour of a purely gaseous cloud nature for G2 using their Brackett-γ observations. They interpreted this source as a bright knot of a larger gas streamer that includes a G2-type object called G1 in a similar orbit, but preceding it by 13 yr. G1 and G2 could be explained as the result of the partial tidal disruption of a star (Guillochon et al. 2014) or as one of many gas clumps created by the collision of stellar winds from the young stars in the Galactic Centre (Burkert et al. 2012; Schartmann et al. 2012). Such dense, cold clumps are copiously produced in the smoothed particle hydrodynamics (hereafter SPH) simulations of the Galactic Centre gas dynamics performed by Cuadra et al. (2005, 2006), Cuadra, Nayakshin & Martins (2008), Cuadra, Nayakshin & Wang (2015, see also Lützgendorf et al. 2015 section 3.3), and could survive pericentre passage if magnetized (McCourt et al. 2015). Moreover, G2's orbit lies on the plane of the 'clockwise disc', defined by the orbits of many young stars (Paumard et al. 2006; Yelda et al. 2014), and its apocentre coincides with the inner rim of that disc. Nevertheless, the SPH technique has a tendency for artificially clumping gas (Hobbs et al. 2013), which raises doubts on how physical the clump formation is in such models. In this context, this work aims to test independently the clump formation as result of colliding stellar winds in the central parsec of the Milky Way.

Massive stars have significant phases of mass-loss through their lives, in which their outflows can be accelerated up to supersonic speeds due to radiation pressure. When two of these stars are at short

⋆E-mail: dcaldero@astro.puc.cl

separations, for example in a binary system, their winds collide and generate a hot slab of shocked gas. Depending on the ability of this gas to cool down, we can identify different regimes. If the shocked gas from both stellar winds cool down rapidly, a cold thin shell will be produced centred at the contact discontinuity (hereafter CD) of the wind–wind interaction zone. This slab will be subject to strong instabilities such as the *non-linear thin shell instability* (hereafter NTSI; Vishniac 1994). In the case that only one of the winds is highly radiative, a cold thin shell will also be formed; but if instabilities are excited they will be damped by the thermal pressure of the hot shocked gas from the other wind (Vishniac 1983). When none of the winds are radiative, the Kelvin–Helmholtz instability (hereafter KHI) is the only instability that can be excited (Stevens, Blondin & Pollock 1992), as it only requires a velocity difference between the winds. However, KHI can also act on top of thin-shell instabilities for radiatively efficient winds.

State-of-the-art numerical modelling (Pittard 2009; van Marle et al. 2010; Lamberts, Fromang & Dubus 2011; Kee, Owocki & ud-Doula 2014) highlights the high computational cost of realistic simulations of unstable colliding wind systems. High spatial and time resolution, plus many physical ingredients, such as gravity, driving of the winds, radiative cooling and orbital motion, are crucial to build realistic models and track the growth of instabilities. In this context, we take an alternative analytical approach and study the thermal evolution of the hot slab created by the colliding winds. This allows us to predict under which conditions, out of a wide parameter space, the NTSI grows, and to estimate the possible resulting clump masses. The paper is divided as follows: Section 2 describes the main cooling diagnostic we use throughout this work and Section 3 presents our model and the results of our parameter space study. In Section 4, we discuss how likely the formation of the G2 cloud is through colliding winds based on our results. Then in Section 5, we discuss the limitations of our results and argue for colliding winds binaries as clump sources in the Galactic Centre. Finally, in Section 6, we present our conclusions and outlook.

2 RADIATIVE COOLING AND THIN SHELLS

The role of radiative cooling is what determines the thickness, density and temperature of the shocked gas layer. If cooling is efficient, the wind collision will produce a dense, thin layer of cold gas, which can easily be subject to the so-called *thin shell instabilities*. In their numerical models, Stevens et al. (1992) identified two such instabilities: the NTSI, later explained analytically by Vishniac (1994), and another damped instability consistent with the earlier description by Vishniac (1983). Moreover, Dgani, Walder & Nussbaumer (1993) described another thin shell instability: the *transverse acceleration instability* that mainly takes place off the two-star axis. Lamberts et al. (2011), modelling unstable colliding winds systems numerically, concluded that the NTSI is the instability that dominates the cold slab evolution due to its large-scale perturbations.

In order to predict whether the wind collision will produce a thin slab, we need to check how fast the shocked gas cools down. Following the description presented in Stevens et al. (1992), the radiative efficiency of shocked stellar winds can be described by the *cooling parameter* χ, which is the ratio of the cooling time-scale to the dynamical time-scale,

$$\chi = \frac{t_{\rm cool}}{t_{\rm dyn}}, \tag{1}$$

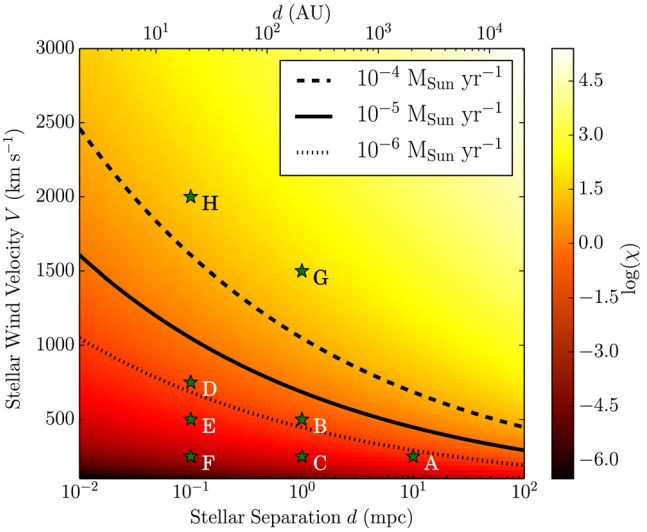

Figure 1. Cooling parameter as colour map on logarithmic scale which was obtained using equation (3) and fixing the mass-loss rate to $10^{-5}\,{\rm M}_{\odot}\,{\rm yr}^{-1}$. It is shown as a function of the stellar separation d (for identical stars) on the x-axis and the stellar wind velocity V on the y-axis. The solid line shows $\chi = 1$ which separates the two regimes: adiabatic (above, $\chi > 1$) and roughly isothermal (below, $\chi < 1$) winds. Dashed and dotted lines show the $\chi = 1$ boundaries for mass-loss rates of 10^{-4} and $10^{-6}\,{\rm M}_{\odot}\,{\rm yr}^{-1}$, respectively. Green stars labelled A–H indicate the parameters of models we study in more detail in Section 3. Notice that 1 mpc $\sim$ 206 au.

where $t_{\rm cool}$ and $t_{\rm dyn}$ are the cooling and the dynamical time-scales, respectively. They are defined as

$$t_{\rm cool} = \frac{3k_{\rm B}T}{2n\Lambda(T)}\ ;\ t_{\rm dyn} = \frac{d_*}{c_{\rm s}}, \tag{2}$$

where T and n are the temperature and number density of the shocked gas, respectively, $\Lambda(T)$ is the cooling function which we will specify in the following section, $k_{\rm B}$ is the Boltzmann constant, d_* is the distance between the star and the CD and $c_{\rm s}$ is the shocked gas sound speed. Therefore, for χ lower than unity, the gas can cool down faster through radiative cooling than through adiabatic expansion. On the contrary, χ larger than one means that radiative cooling is not efficient. Following Stevens et al. (1992), but using a cooling function that depends on metal abundance (specified in Section 3.2) and temperature rather than being constant (see equation 10) we can calculate the cooling parameter for each stellar wind given its properties,

$$\chi \approx \frac{1}{2}\frac{V_8^{5.4} d_{*12}}{\dot{M}_{-7}}, \tag{3}$$

where V_8 is the terminal wind speed V in units of $1000\,{\rm km\,s^{-1}}$, d_{*12} is the distance between the star and the CD d_* in units of 10^{12} cm and $\dot{M}_{-7}$ is the mass-loss rate $\dot{M}$ in units of $10^{-7}\,{\rm M}_{\odot}\,{\rm yr}^{-1}$. In Fig. 1, we show χ as a function of V and the stellar separation of identical stars $d = 2d_*$ for $\dot{M} = 10^{-5}\ {\rm M}_{\odot}\,{\rm yr}^{-1}$ fixed, which is the typical value for the Wolf–Rayet stars in the Galactic Centre (see Section 4). We have highlighted the boundary $\chi = 1$ to separate the two cooling regimes. We will concentrate on the $\chi < 1$ region, which is where the NTSI excitation is possible.

3 NTSI AND CLUMP FORMATION

As discussed in the previous section, if the slab gas can cool down rapidly, different thin shell instabilities can be excited. The

dominant instability is the NTSI, which is the result of the misalignment of the thermal pressure within the cold slab (which always acts perpendicular to the slab) and the ram pressure of the wind (always acting parallel to the wind direction). This generates a convergent flux on to perturbation knots where gas accumulates, and a subsequent mixing of both phases of the material. In this section, we use the description of Vishniac (1994) to calculate the allowed wavelength range of the NTSI which can grow.

3.1 Range of unstable wavelengths

The growth of the NTSI can occur only for wavelengths shorter than those coordinated by sound waves: $\lambda < c_s t$. On the other hand, the shortest unstable wavelength is given by the slab thickness $l(t)$, i.e. $\lambda \gtrsim 2l(t)$. Moreover, the NTSI can grow only if the slab perturbation has an initial amplitude at least comparable to the thickness of the layer. Notice that the criteria depend on the time t elapsed since the formation of the slab. The thickness of the slab generated by isothermal flows is given by $l(t) = 2V_n t$, where $V_n = V/(\mathcal{M}^2 - 1)$ is the velocity at which the slab thickens, $\mathcal{M} = V_s/c_s$ is the Mach number and $V_s = V + V_n$ is the shock speed. Notice that for the limit of high Mach number $V_s \approx V$, and that the more supersonic the shock, the slower the slab increases its width.

3.2 Analytic model

In our model, we consider two identical stars that are fixed in space. They have a given mass-loss rate and wind terminal velocity, and are separated by a given distance. Respectively, these three quantities $\dot{M}$, V and d are the input parameters of the model. We follow the time evolution of the gas within the slab formed when the winds collide by studying its integrated density and thermal evolution, including a radiative cooling term. We define the relevant densities as

$$\Sigma_{\rm slab} = \rho_{\rm slab} L, \tag{4}$$

where $\rho_{\rm slab}$ is the volumetric density inside the slab, $\Sigma_{\rm slab}$ is the surface density of the slab and L is the width of the slab. All these quantities evolve and we study them as a function of their age, i.e. the time after the wind collision. As we are studying a symmetric system (identical stars with identical winds), we model one side of the system. Therefore, $L(t)$ will be the distance from the CD to the discontinuity of the shocked and the free-wind region. As the slab is supported by thermal pressure, in this point the thermal and the wind ram pressure have to be balanced, which is a reasonable assumption considering that the thermal energy is negligible in the free-wind region that is highly supersonic ($\mathcal{M} \geq 20$). From this model, we can write the hydrodynamical equations as follows:

$$\frac{\rm d}{{\rm d}t}\Sigma_{\rm slab} = \rho_{\rm wind} V, \tag{5}$$

$$P_{\rm slab} = \rho_{\rm wind} V^2, \tag{6}$$

$$\frac{3k_{\rm B}}{2\mu m_{\rm H}}\frac{\rm d}{{\rm d}t}(\Sigma_{\rm slab} T_{\rm slab}) = H_{\rm shock} + S_{\rm cool}, \tag{7}$$

where $P_{\rm slab}$ is the pressure in the slab, μ is the mean molecular weight, $m_{\rm H}$ is the proton mass, $H_{\rm shock}$ is the mechanical heating term (i.e. kinetic energy flux from the wind per unit surface) and $S_{\rm cool}$ is the energy dissipation term through radiative cooling. These source terms are given by

$$H_{\rm shock} = \frac{1}{2}\rho_{\rm wind} V^3, \tag{8}$$

$$S_{\rm cool} = \frac{\Sigma_{\rm slab}\rho_{\rm slab}}{\mu^2 m_{\rm H}^2}\Lambda(T_{\rm slab}), \tag{9}$$

where the cooling function $\Lambda(T)$ is an analytical approximation for optically thin radiative cooling made by Cuadra et al. (2005) following Sutherland & Dopita (1993),

$$\Lambda(T) = 6.0 \times 10^{-23}\left(\frac{Z}{3}\right)\left(\frac{T}{10^7{\rm K}}\right)^{-0.7} {\rm erg\ cm^3\ s^{-1}}, \tag{10}$$

where Z is the metal abundance relative to solar. We set $Z = 3$ and discuss the impact of this choice in Section 5.1.2. Combining the system of equations (5)–(9) and assuming an ideal gas $P_{\rm slab} = \rho_{\rm slab} k_{\rm B} T_{\rm slab}/(\mu m_{\rm H})$, we can derive a single differential equation that describes the thermal evolution of the slab:

$$\frac{3k_{\rm B}}{2\mu m_{\rm H}}\frac{\rm d}{{\rm d}t}T_{\rm slab} = \frac{1}{2}\frac{V^2}{t} - \frac{\rho_{\rm wind} V^2}{k_{\rm B}\mu m_{\rm H}}\frac{\Lambda(T_{\rm slab})}{T_{\rm slab}} - \frac{3k_{\rm B}}{2\mu m_{\rm H}}\frac{T_{\rm slab}}{t}. \tag{11}$$

The first term on the right-hand side represents the mechanical heating of the shock; the second, the radiative cooling; and the third, the work done by the slab. Furthermore, the slab density can be easily computed making use of equation (6) and the ideal gas equation of state. Thus, the slab width time evolution can be calculated using equations (4) and (5) to obtain

$$\frac{\rm d}{{\rm d}t}[\rho_{\rm slab}(t) L(t)] = \rho_{\rm wind} V \Rightarrow L(t) = \frac{\rho_{\rm wind}}{\rho_{\rm slab}(t)} V t. \tag{12}$$

From this expression, we note that if the slab does not cool down (i.e. the slab density remains roughly constant), the slab will increase its width linearly with time; on the contrary, if the slab gets denser very rapidly it may overcome the linearity dependence with time and collapse as a thin shell which grows very slowly due to the fact that $\rho_{\rm wind}/\rho_{\rm slab} \ll 1$. With this analysis, we can calculate the NTSI growth criteria as a function of the age of the slab (or time after the wind collision). Although the model is simple, it can provide us with information about the instabilities that can take place in order to estimate sizes and masses of the possible clumps. It is important to mention that throughout this analysis we are not attempting to follow the evolution of the instability, but to study under which conditions it can be triggered.

3.3 Parameter study

Using the previously described procedure, we explored the parameter space shown in Fig. 1. We first present in detail a few relevant and representative examples (see Table 1). In all these models, we kept $\dot{M} = 10^{-5}$ M$_\odot$ yr^{-1} fixed and stopped the calculation after the gas has cooled down significantly, reaching a temperature of 10^4 K.

Table 1. Parameters of each model presented in this work. Column 1: model name. Column 2: wind terminal velocity. Columns 3 and 4: stellar separation in mpc and au, respectively. Column 5: cooling parameter χ estimated from equation (3) and $\dot{M}$ fixed to 10^{-5} M$_\odot$ yr^{-1}.

Model	V (km s^{-1})	d (mpc)	d (au)	χ
A	250	10.0	2.06×10^3	0.0433
B	500	1.0	2.06×10^2	0.1827
C	250	1.0	2.06×10^2	0.0043
D	750	0.1	2.06×10^1	0.1632
E	500	0.1	2.06×10^1	0.0183
F	250	0.1	2.06×10^1	0.0004
G	1500	1.0	2.06×10^2	69.89
H	2000	0.1	2.06×10^1	32.57

This is a reasonable temperature floor because of the presence of many hot, young stars emitting ionizing radiation that prevents the temperature to drop to lower values.[1]

The time evolution of the unstable wavelength criteria for the NTSI is shown for all models in Figs 2 and 3. Fig. 2 shows the models with $\chi < 1$. Here, for most of the evolution of the slab, the upper limit (solid blue line) is *below* the lower limit (dashed green line), meaning that the instability cannot grow as there is no unstable wavelength range. Only at the very end of each calculation the upper limit is above the lower limit and therefore the instability develops. The sudden drop in the lower limit is due to the fast slab gas compression once cooling becomes much more efficient as the temperature decreases. In all these cases, we registered the unstable length range and the final density values in Table 2. It is important to remark that for all these cases we remain in the thin shell regime, i.e. $L/d \ll 1$. Therefore, we do not expect radiative cooling to be faster than the thermal response of the slab, making our assumption of pressure equilibrium at the shock valid.

Assuming spherical symmetry, we used the unstable wavelength range to compute a range of masses for clumps (see Table 2). However, these values must be interpreted only as upper limits, because we have assumed the clump radii to be about the size of the unstable wavelengths, which is probably an extreme case. From the results, we see that larger stellar separations will result in larger clumps. However, these clumps are less dense due to the winds being significantly diluted before they collide. On the contrary, smaller separations produce smaller and denser clumps. The combination of these two factors sets the clump masses in a non-trivial manner. Our results show that Model A, Model B and Model D could generate clumps with masses $>0.1\,\mathrm{M}_{\oplus}$ and the most massive ones would be generated by Model B, reaching G2-like masses ($\sim 5\,\mathrm{M}_{\oplus}$).[2]

On the other hand, Fig. 3 shows the models with $\chi > 1$, in which we see that the width of the slab (dashed green line) becomes larger than the stellar separation (dotted red line) before there is an unstable wavelength range. Thus, we deem these models not physical, as our treatment cannot describe these systems properly, and we expect no clump formation through NTSI for this parameter range.

Although these results show that clump formation might occur for the $\chi < 1$ models, we need to check on which time-scales this process takes place. Vishniac (1994) showed that the NTSI growth time-scale τ is given by

$$\tau = \frac{\lambda^{1.5}}{\zeta^{0.5} c_{\mathrm{s}}}, \tag{13}$$

where ζ is the initial amplitude of the perturbation. If we assume $\zeta \sim \lambda$, the growth time-scale is simply given by the sound crossing time-scale, i.e. $\tau \sim \lambda/c_{\mathrm{s}}$. Estimations of τ under this assumption for each of our models are presented in Table 2. Moreover, we present the clump masses as a function of the growth time-scale for each model in Fig. 4, where we see that models with shorter stellar separations ($d = 0.1$ mpc in green lines) tend to be the ones that can create clumps the quickest. This is due to these winds being less diluted when they collide, making the cooling more efficient. We can compensate this effect by increasing the wind speed, as a hotter slab would take longer to radiate most of its energy away. For example, comparing cases C and E (solid blue and dashed green, respectively) we see that the combination of different stellar separations and different wind speeds produces clump formation on roughly the same time-scale.

An interesting point is that the models that can create the most massive clumps have significantly different parameters. This can be explained by the fact that clump masses are proportional to λ^3, thus the most massive clump possibly generated would have a mass $M \propto \lambda^3_{\mathrm{max}}$. Moreover, the upper limit of the unstable wavelength range of the NTSI is given by the sound crossing distance, i.e. $\int c_{\mathrm{s}} \mathrm{d}t$ integrated over the age of the slab when it reaches 10^4 K. This tells us that how massive clumps can be, depends on how long it takes for the slab to cool down and become unstable. Then, either high-velocity winds and/or larger separations would produce more massive clumps. In order to illustrate this explicitly, we have explored our parameter space more extensively, modelling 45 systems in total. We show this in Fig. 5 as a function of the input parameters of our model. The left- and right-hand panels present the lower and upper limits of the clump mass range, respectively. Here, it is easy to see that for larger separations and/or higher wind velocities the minimum and maximum clump masses are larger.

We repeated the previous analysis using different mass-loss rate values, 10^{-6} and $10^{-4}\,\mathrm{M}_{\odot}\,\mathrm{yr}^{-1}$, finding that for lower $\dot{M}$ values, clumps can be more massive for the same combination of (d, V), as a less dense slab makes the cooling less efficient, but we would need shorter distances and/or slower winds in order to get radiative winds in the first place, as the $\chi = 1$ line moves down in the parameter space (see Fig. 1). On the contrary, increasing $\dot{M}$ we obtain less massive clumps for the same (d, V), as a denser slab makes the cooling more efficient, but this would allow larger separations and/or faster winds to generate radiative winds, as the $\chi = 1$ line moves up in the parameter space.

To study which clumps will actually form, we take into account equation (13) that shows that shorter wavelengths grow faster. Therefore, for any model we would expect first the formation of the lightest possible clumps. On longer time-scales, larger wavelengths would also act, accumulating the small clumps and possibly merging them to create more massive clumps. To actually predict a clump mass distribution, we require numerical simulations. We defer that study to a forthcoming work.

In general, we find that for parameters closer to $\chi = 1$ (black dashed line in Fig. 5), we would expect more massive clumps to be formed. However, we do not know exactly at what point our approach becomes unphysical as we go closer to the adiabatic regime, as seen in models G and H (see Fig. 3). Thus, it is more sensible to explore the parameter space close to $\chi = 1$ with numerical simulations. This is why we explored values up to $\chi = 0.5$ only (black solid line). Despite this, we see that clump masses span a very wide range of masses and that the creation of clumps as massive as G2 is possible.

4 COLLIDING STELLAR WINDS IN THE GALACTIC CENTRE

We have studied the parameter space for close pairs of mass-losing stars, checking whether we expect them to form clumps through the NTSI, plus estimating the allowed range of sizes and masses for those clumps. Now, we apply this model to the stars in the central parsec of the Milky Way, as the NTSI could be excited for the colliding winds of massive stars, and explain the origin of the G2 cloud. Our model assumes that the stars are stationary and that the pairs are identical. The first assumption is justified as the time-scales involved in the instability ($\lesssim$10 yr, e.g. Fig. 4) are typically much shorter than

[1] We also tested stopping the cooling at 10^5 K, finding that density values are systematically smaller by one order of magnitude.

[2] G2 could also have formed by mergers of smaller clumps, but we cannot address this option with our current approach.

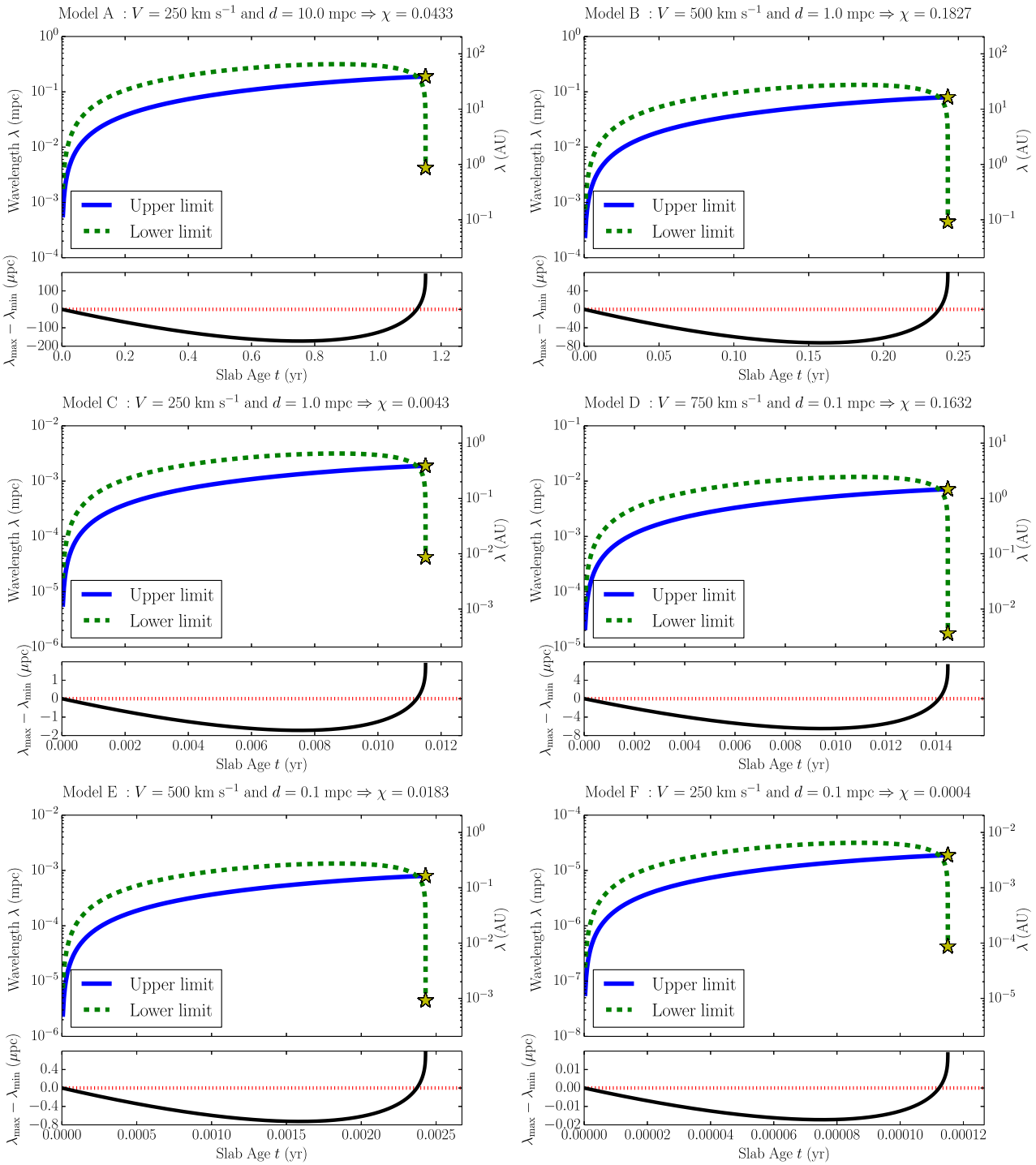

Figure 2. Evolution of the NTSI wavelength criteria for the radiative models ($\chi < 1$). On the upper panels, we show the time evolution of the upper and lower limits of unstable wavelengths for the NTSI obtained from our analytic prescription. Instabilities can grow only at the end of each time evolution, when a range of allowed wavelengths exists. Yellow stars represent the final state of the system when the gas has reached 10^4 K. On the lower panels, the thick black line represents the difference between the upper and lower limits, $\lambda_{max} - \lambda_{min}$, and the dotted red line is fixed at zero for reference. Note the different scales in the *x*- and *y*-axis between models.

the duration of close stellar encounters of mass-losing stars in the Galactic Centre (see Table 4). The second issue is partially addressed in Section 4.3. Our sample of mass-losing stars in the inner parsec of the Galaxy is the same used in the numerical models by Cuadra et al. (2008, 2015) and it is listed in Table 3. For most of the stars, the wind properties were taken from Martins et al. (2007), who fitted stellar atmosphere models to spectra obtained with SINFONI at the VLT. For the rest, the wind properties were assigned by Cuadra et al. (2008) based on their similarity to other stars whose spectra were properly modelled by Martins et al. (2007). The

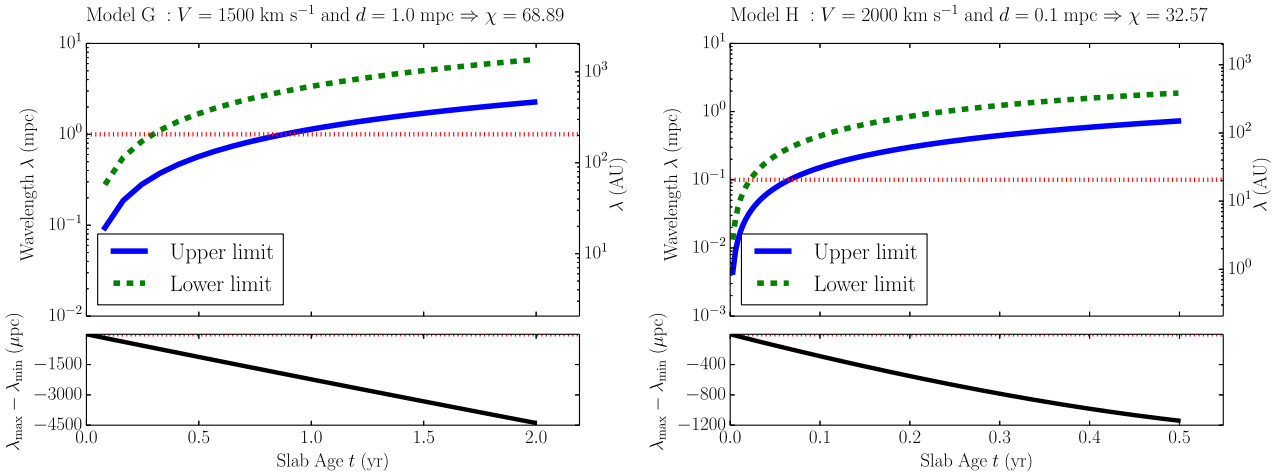

Figure 3. Same as Fig. 2 but for the adiabatic models ($\chi > 1$) G and H. At some point the models become unphysical, as the slab width is comparable to the stellar separation (red dotted line). We do not expect NTSI excitation for these models.

Table 2. Results of our estimates for each model. Column 1: model name. Columns 2 and 3: unstable wavelength range obtained from our analysis in mpc and au, respectively. Column 4: slab density obtained estimated from our calculations. Column 5: clump mass range computed assuming spherical clumps and uniform density with radius equal to the instability wavelengths. Column 6: growth time-scale estimated assuming an initial amplitude equal to the instability wavelength and the slab sound speed at the temperature floor (10^4 K).

Model	Unstable λ (mpc)	Unstable λ (au)	ρ_{slab} (g cm^{-3})	Clump mass range ($M_\oplus$)	Growth time-scale (yr)
A	(4–190) $\times 10^{-3}$	(8–390) $\times 10^{-1}$	2.4×10^{-18}	3.6×10^{-6}–3.3×10^{-1}	(3–120) $\times 10^{-1}$
B	(5–800) $\times 10^{-4}$	(1–160) $\times 10^{-1}$	4.7×10^{-16}	8.8×10^{-7}–4.9×10^{0}	(3–50) $\times 10^{-1}$
C	(4–190) $\times 10^{-5}$	(8–390) $\times 10^{-3}$	2.4×10^{-16}	3.6×10^{-10}–3.3×10^{-5}	(3–120) $\times 10^{-3}$
D	(2–710) $\times 10^{-5}$	(4–1460) $\times 10^{-3}$	7.1×10^{-14}	8.5×10^{-9}–5.3×10^{-1}	(1–470) $\times 10^{-3}$
E	(5–800) $\times 10^{-6}$	(1–160) $\times 10^{-3}$	4.7×10^{-14}	8.8×10^{-11}–4.7×10^{-4}	(3–50) $\times 10^{-4}$
F	(4–190) $\times 10^{-7}$	(8–390) $\times 10^{-5}$	2.4×10^{-14}	3.6×10^{-14}–3.3×10^{-9}	(3–120) $\times 10^{-5}$
G	–	–	2.6×10^{-19}	–	–
H	–	–	2.6×10^{-21}	–	–

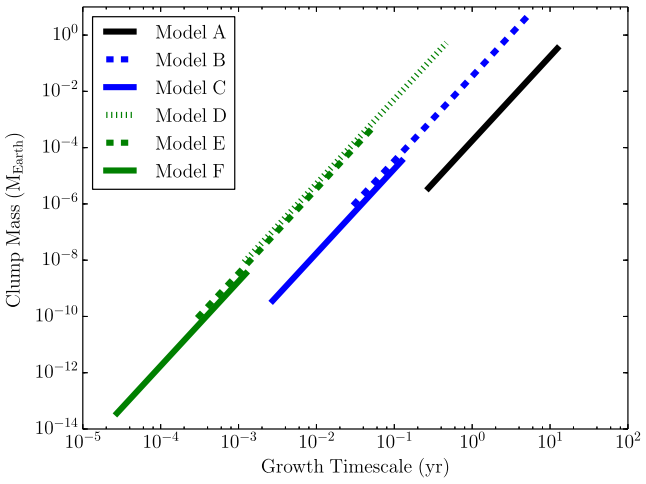

Figure 4. Clump masses (assuming spherical symmetry) generated through the NTSI, as a function of the instability growth time-scale (assuming an initial amplitude comparable to the instability wavelength). Different stellar separations are shown with different colours: green, blue and black stand for 0.1, 1 and 10 mpc (20.6, 206 and 2060 au), respectively, while different wind velocities are shown with different line styles: solid, dashed and dotted represent 250, 500 and 750 km s^{-1}.

typical uncertainty in the parameters derived by Martins et al. (2007) is ∼100 km s^{-1} for the velocities and ∼0.2 dex for the mass-loss rates, small enough not to influence our conclusions.

4.1 Radiative cooling diagnostic

We first estimate the critical separation between stars in order for their winds to be radiatively efficient. We use the previously defined *cooling parameter* χ, and compute the radiative-to-adiabatic transition separation equating $\chi = 1$,

$$d_*^{\rm cool} = 2 \times 10^{12} {\rm cm} \, \frac{\dot{M}_{-7}}{v_8^{5.4}}. \quad (14)$$

Pairs of identical stars with separations $d > 2d_*^{\rm cool}$ will produce adiabatic shocks, while those with $d < 2d_*^{\rm cool}$ will result in radiatively cooled shocks. The value of $2d_*^{\rm cool}$ is included in Table 3, and is also plotted as a function of the wind momentum fluxes in Fig. 6. Note that, for any pair of stars, d changes with time as they orbit in the Galactic Centre, therefore colliding wind stars can go through both regimes. Star 33E has the largest value of $d_*^{\rm cool}$. Encounters involving this star with similar ones at 10 mpc scales should result in the formation of cold slabs. For the rest of the sample, we see that only for separations below 0.1–1 mpc (20–206 au) their winds would be radiatively efficient. Such short separations are in the range of close binary systems (see Section 5.2).

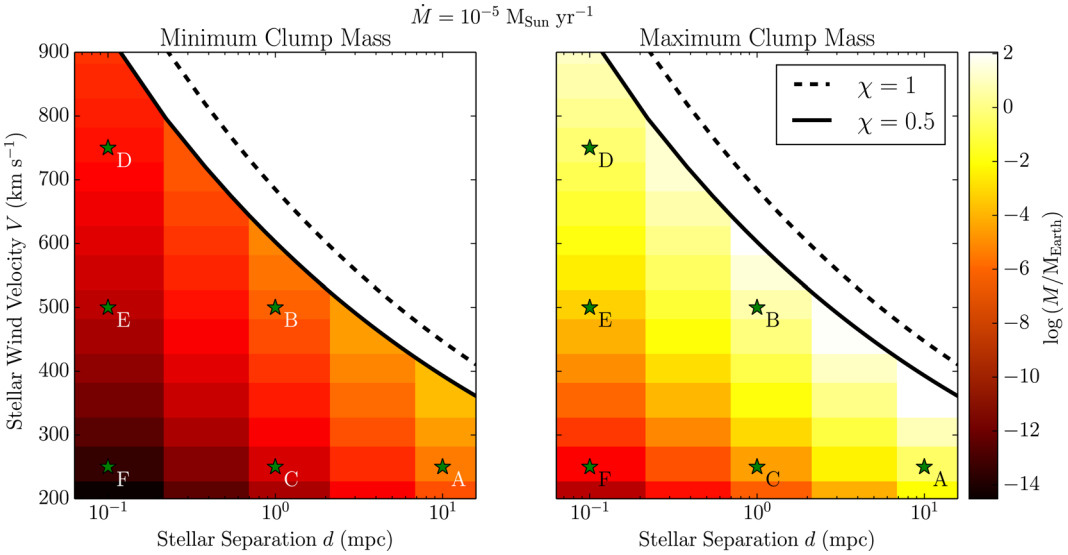

Figure 5. Parameter space (d, V) with $\dot{M} = 10^{-5}$ M$_\odot$ yr^{-1} fixed, displaying clump masses (colours) formed through NTSI obtained with our model. The left- and right-hand panels show the minimum (lower limit) and maximum (upper limit) clump mass for a given combination of parameters, respectively. Green star symbols show the models we previously studied in detail. The solid and dashed black lines stand for $\chi = 0.5$ and $\chi = 1$, respectively.

4.2 Mass-losing stars encounters in the Galactic Centre

Now we turn our attention to the stellar orbits in the Galactic Centre, to study how often close encounters between single mass-losing stars are produced. To do so, we ran a simple, Newtonian gravity, test-particle simulation to follow the stars around Sgr A*. This approximation is correct, as the distances from the stars to Sgr A* are too large for relativistic effects to be important, and the time-scale for stellar scattering to be relevant is much longer than the period we are interested in (see Alexander 2005). We ran the models for 10^4 yr, which is already a much longer time-scale than the expected lifetime of a cloud like G2 (Burkert et al. 2012).

We only registered encounters of stellar pairs at distances shorter than 10 mpc (2060 au) based on our parameter space study, noting the minimum distance of the close passage $d_{\rm min}$ and the duration of the encounter (i.e. the time stars are closer than 10 mpc). As initial conditions we used the 3D velocities and 2D sky positions observed by Paumard et al. (2006), meanwhile the unobservable z-coordinate was chosen using different assumptions for the orbital distribution. We used the three different models from the work by Cuadra et al. (2008) to obtain the z-coordinate of our young star sample: *Min-ecc*, *1Disc* and *2Discs*. *Min-ecc* uses the z-coordinate values that minimize the orbital eccentricities, *1Disc* assumes roughly half of the stars are in the well-defined clockwise disc (Beloborodov et al. 2006), and *2Discs* assumes the existence of both clockwise and counterclockwise discs. The results of this procedure are summarized in Table 4, where we see that over a 10^4 yr period, there is at most one encounter with a $\sim$1 mpc separation.[3] From the typical encounter duration of $\sim$50 yr and our integration time, we can estimate a rough probability of producing G2 through encounters of single stars as 0.5 per cent.

[3] Notice that this "encounter" happens between stars 13E2 and 13E4, which might be bound together by a dark mass (Fritz et al. 2010), not included in our calculations. That dark mass would, however, likely increase the encounter duration.

4.3 Asymmetric mass-losing stars encounters

For simplicity, we have only analysed collisions of identical stellar winds. However, in reality we will typically have encounters between stars with different wind properties. To study such cases, detailed numerical simulations are needed, such as those performed by Pittard (2009), van Marle et al. (2010) and Lamberts et al. (2011). These authors have shown that even a small velocity difference in the colliding winds can excite the KHI. This would mix two-phase material on top of other instabilities that can take place simultaneously. Although all these processes can be very complicated to track analytically, based on our work we can give a qualitative description of possible scenarios that can take place for asymmetric close encounters. Stellar wind encounters are characterized by their momentum flux ratio (Lebedev & Myasnikov 1990),

$$\eta = \frac{\dot{M}_2 V_2}{\dot{M}_1 V_1}, \tag{15}$$

where the subscript 2 stands for the weaker wind and 1 for the stronger one, so $\eta \leq 1$ by definition. Notice that η is independent of the stellar separation, provided this is large enough to allow the winds to reach their terminal velocities.

For $\eta \neq 1$, the interaction zone of the shocked gas bends towards the weaker star. The CD distance to the weaker wind star will be given by

$$R_2 = \frac{\sqrt{\eta}}{1+\sqrt{\eta}} d. \tag{16}$$

Then, the CD will be located closer to the weaker star for systems with smaller η. Furthermore, the weaker wind will be less diluted before the collision producing a denser slab (compared to systems with same η but different stellar separation). In this way, stars with large momentum fluxes in their winds can be important in asymmetric encounters as they could 'force' weaker winds to radiate their energy rapidly, which would result in radiative shocks. In Fig. 6, we highlighted the stars with largest momentum fluxes in their winds, including their names on the plot. Encounters of these stars with others, of the left-hand side of the plot, will produce encounters

Table 3. Galactic Centre mass-losing star sample taken from Martins et al. (2007) and Cuadra et al. (2008). Column 1: star ID. Column 2: star name. Both from Paumard et al. (2006). Column 3: stellar wind terminal velocity. Column 4: stellar mass-loss rate. Columns 5 and 6: twice the radiative-to-adiabatic wind transition distance computed from equation (14) in mpc and au, respectively.

ID	Name	V (km s^{-1})	$\dot{M}$ ($M_\odot$ yr^{-1})	$2d_*^{\rm cool}$ (mpc)	(au)
19	16NW	600	1.12×10^{-5}	2.29	472
20	16C	650	2.24×10^{-5}	2.97	612
23	16SW	600	1.12×10^{-5}	2.29	472
31	29N	1000	1.13×10^{-5}	0.15	31
32	16SE1	1000	1.13×10^{-5}	0.15	31
35	29NE1	1000	1.13×10^{-5}	0.15	31
39	16NE	650	2.24×10^{-5}	2.97	612
40	16SE2	2500	7.08×10^{-5}	0.01	2
41	33E	450	1.58×10^{-5}	15.28	3148
48	13E4	2200	5.01×10^{-5}	0.01	2
51	13E2	750	4.47×10^{-5}	2.74	564
56	34W	650	1.32×10^{-5}	1.75	361
59	7SE	1000	1.26×10^{-5}	0.16	33
60	–	750	5.01×10^{-6}	0.31	64
61	34NW	750	5.01×10^{-6}	0.31	64
65	9W	1100	4.47×10^{-5}	0.35	72
66	7SW	900	2.00×10^{-5}	0.46	95
68	7W	1000	1.00×10^{-5}	0.13	27
70	7E2	900	1.58×10^{-5}	0.36	74
71	–	1000	1.13×10^{-5}	0.15	31
72	–	1000	1.13×10^{-5}	0.15	31
74	AFNW	800	3.16×10^{-5}	1.37	282
76	9SW	1000	1.13×10^{-5}	0.15	31
78	B1	1000	1.13×10^{-5}	0.15	31
79	AF	700	1.78×10^{-5}	1.58	325
80	9SE	1000	1.13×10^{-5}	0.15	31
81	AFNWNW	1800	1.12×10^{-4}	0.06	12
82	Blum	1000	1.13×10^{-5}	0.15	31
83	15SW	900	1.58×10^{-5}	0.36	74
88	15NE	800	2.00×10^{-5}	0.87	179

with small η and short distances R_2 from the weaker star to the CD. For each of the encounters we registered in the previous subsection, we calculated the momentum flux ratio and the R_2 value. We can now modify the definition of the cooling parameter (equation 3), so it uses the distance R_2 at which the CD is expected to form in the asymmetric close encounters,

$$\chi_{\rm asym} \approx \frac{1}{2}\frac{V_8^{5.4} R_{2,12}}{\dot{M}_{-7}}, \tag{17}$$

where $R_{2,12} = R_2/10^{12}$ cm. Since R_2 is always a fraction of $d/2$, the density of the weaker wind will be higher at that position compared to the symmetric case and the slab will be able to radiate its energy away more rapidly. All these estimates are included in Table 4. From those results, we can check that for two of our models (*1Disc* and *Min-ecc*) there is only one encounter where the weaker wind produces a cold slab that might become unstable, while in the other case (*2Discs*), there are four such encounters. The difference is at least partially due to the fact that in the *2Discs* case the stars are closer together and more encounters are produced in general. These systems deserve more study because they could be clump sources. It is important to remark that, in the asymmetric case, on one side of the CD we have a thin shell while on the other we have the hot shocked gas of the stronger wind. The latter tends to stabilize any instability possibly excited, so even if $\chi_{\rm asym} < 1$ there might be no clump formation. Also notice that all these estimates were done under the assumption that the stars are separated well enough in order to accelerate their winds up to their terminal velocities. However, for extreme values of η that might not be the case.

5 DISCUSSION

5.1 Limitations and uncertainties in the model

Although our model has been very useful to test the likelihood of clump formation in stellar wind shocked gas, there are two important assumptions we have to consider before comparing with other works, especially with two- or three-dimensional models.

5.1.1 *The planar winds assumption*

Our model considers planar shocks, rather than more realistic spherical wind collisions. A planar shock geometry is a good approximation for the wind collision at the apex (i.e. at the CD and two-star axis intersection), where the gas effectively moves along the axis joining both stars. Off this axis, the winds will have a perpendicular velocity component, and the planar approximation breaks down. Moreover, the off-axis velocity will prevent the material from accumulating in the slab. Nevertheless, the well-modelled apex is arguably the most interesting location of the wind collision for us, as this is where we expect the most massive clumps to form. As shown in Fig. 5, as long as we stay in the radiatively efficient regime, higher values of χ generate more massive clumps. So far, we have defined χ using the wind speed and the distance between the stars, which is only appropriate along the two-stars axis. In a more realistic model, χ changes along the CD, decreasing from the apex as we show below.

Let us define a more general cooling parameter as $\chi = \chi(\theta)$, where θ is the angle between the two-star axis and a line connecting one star and an arbitrary point P on the CD. The distance from the star to P will be given by $d'_* = d_*/\cos\theta$. Furthermore, the shock at P will be weaker than at the apex, as only the component perpendicular to the CD will contribute to it. This component will be given by $V' = V\cos\theta$. Using these quantities, we can generalize equation (3) obtaining

$$\chi(\theta) = \frac{1}{2}\frac{V_8^{5.4} d_{*12}}{\dot{M}_{-7}}(\cos\theta)^{4.4} = \chi_\perp(\cos\theta)^{4.4}, \tag{18}$$

where $\chi_\perp$ is the cooling parameter at the apex, as previously defined in equation (3). From this new expression, we see that in general, $\chi(\theta) \leq \chi_\perp$, recovering equation (3) when $\theta = 0$ as expected. Thus, away from the apex the cooling parameter decreases, and according to our results, we expect the creation of less massive clumps. With this in mind, the clump masses we quote are the largest we can expect from a given wind collision and they would form near the apex where the planar-wind assumption is accurate.

5.1.2 *Impact of metallicity on radiative cooling*

Different metallicities result in different cooling time-scales, which in turn modify the sizes and masses of the clumps. As there is no agreement on the metallicity measurements for the massive stars in the Galactic Centre (see the review by Genzel et al. 2010), we have set $Z = 3\,Z_\odot$, following Cuadra et al. (2005) and close to the values

Table 4. Galactic Centre mass-losing star encounters at <10 mpc (2060 au). Column 1: initial conditions model name. Column 2: IDs of the stars in the encounter. For each pair, the asterisk symbol (*) marks the star with the weaker wind (i.e. smaller momentum flux). When no asterisk is shown, both stars have the same momentum flux. Columns 3 and 4: minimum stellar separation in the encounter in mpc and au, respectively. Column 5: time stars are closer than 10 mpc (2060 au). Column 6: wind momentum flux ratio estimated from equation (15). Columns 7 and 8: CD distance to the weaker wind star calculated from equation (16) in mpc and au, respectively. Column 9: weaker wind cooling parameter obtained from equation (17). Column 10: whether the weaker wind is radiative or not at the minimum stellar separation of the encounter.

Model	Stars	$d_{\rm min}$		Duration	η	R_2		Weaker wind	Thin shell?
		(mpc)	(au)	(yr)		(mpc)	(au)	$\chi_{\rm asym}$	($\chi_{\rm asym} < 1$)
1Disc									
	40 – 60*	9.2	1895	10	0.021	1.16	239	7.581	NO
	48 – 60*	4.0	824	80	0.034	0.62	128	4.052	NO
	48 – 51*	1.0	206	1200	0.304	0.36	74	0.260	YES
	51 – 60*	6.0	1236	70	0.112	1.50	309	9.797	NO
2Discs									
	19* – 48	3.0	618	15	0.061	0.59	122	0.519	YES
	19* – 51	7.0	1442	20	0.200	2.16	445	1.889	NO
	19* – 48	2.0	412	220	0.061	0.40	82	0.347	YES
	19* – 51	4.0	824	20	0.200	1.24	255	1.080	NO
	19* – 51	9.5	1957	10	0.200	2.94	606	2.564	NO
	20 – 32*	8.0	1648	60	0.776	3.75	773	51.16	NO
	31 – 72	7.5	1545	20	1.000	3.75	773	51.20	NO
	39* – 51	2.0	412	15	0.434	0.79	163	0.534	YES
	41* – 48	9.0	1854	10	0.065	1.83	377	0.240	YES
	48 – 51*	5.0	1030	550	0.304	1.78	367	1.297	NO
Min-ecc									
	23* – 41	8.0	1648	50	0.945	3.94	812	3.442	NO
	48 – 51*	1.0	206	1200	0.304	0.36	74	0.260	YES
	48 – 60*	4.0	824	80	0.034	0.62	128	4.058	NO
	48 – 61*	6.0	1236	20	0.034	0.93	192	6.084	NO
	51 – 60*	6.0	1236	70	0.112	1.50	309	9.797	NO
	51 – 61*	7.5	1545	25	0.112	1.88	387	12.25	NO

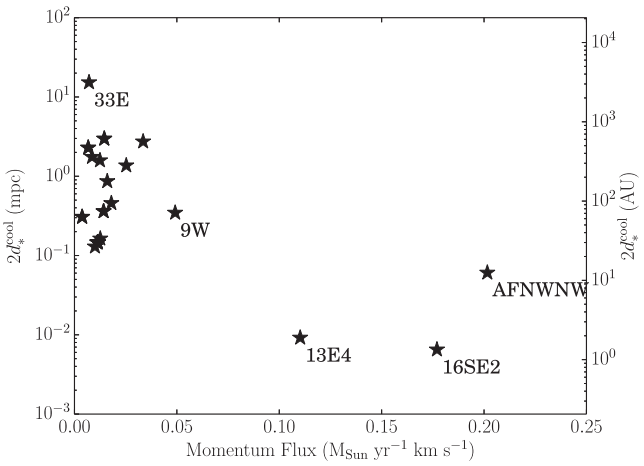

Figure 6. Critical stellar separation in order for their winds to be efficiently radiative (i.e. their collision could produce a *thin shell*) as a function of their wind momentum flux ($\dot{M} \times V$). The sample plotted corresponds to the one shown in Table 3. Stars with large momentum fluxes are labelled, as they can be important in asymmetric encounters 'forcing' weaker winds to radiate their energy rapidly, resulting in radiative shocks. Star 33E is also labelled as it has the largest value of $d_*^{\rm cool}$.

Martins et al. (2007) studied. However, in order to quantify the sensitivity to our choice, we also produced models with metallicities of $Z_\odot$ and 5 $Z_\odot$ in the analytical cooling function we use (see equation 10). We found changes of a factor ∼2 in the clump sizes, which translate in a factor ∼8 for the clump masses. As expected, a lower metallicity value increases the cooling time-scale, and vice versa. Nevertheless, these changes in the metallicity do not result in switching the wind regimes for the system we have analysed (e.g. from radiative to adiabatic or in the opposite direction) as the impact on the cooling parameter is not very strong for the metallicity values we have tested. Thus, we are confident that our results do not depend strongly on our chosen metallicity. Still, one should be cautious when comparing with other works which could have used other metallicity values, and therefore another cooling function.

5.2 Binary stars

Based on our results, clump formation seems not very likely to occur in the environment of the Galactic Centre, due to either symmetric or asymmetric stellar encounters. However, we have not studied a case that probably deserves more attention: *colliding winds binary systems*.

As shown in Section 4.1, the formation of cold slabs typically requires stellar separations below 1 mpc. While those separations are not often achieved in stellar encounters of single stars, they are easily reached by close binaries. The census of young massive binary stars in the Galactic Centre is still incomplete, but the recent study by Pfuhl et al. (2014) increased to three the amount of confirmed binary systems: (i) IRS 16SW, a 19.5-d period Ofpe/WN9 eclipsing contact binary (Martins et al. 2006), (ii) IRS 16NE, a 224-d period Ofpe/WN9 binary and (iii) E60,[4] a 2.3-d eclipsing contact

[4] The star with ID 60 in Table 3.

Wolf–Rayet binary. The inferred separations of these binary systems are of the order of 10 μpc and below. That, together with the wind properties listed in Table 3, could make these three binaries very effective sites for clump formation. IRS 16SW is of particular interest, as it has a clockwise orbit that roughly coincided with G2's at the latter's apocentre. Notice that the wind properties of these stars were assigned by Cuadra et al. (2008) as mentioned in Section 4. However, we would not expect any important wind component to be substantially faster, as it would show up as broader lines in the spectra. Additionally, from the estimations by Pfuhl et al. (2014) we expect an overall ∼30 per cent spectroscopic binary fraction for the massive OB/Wolf-Rayet stars in the Galactic Centre. Thus, even though our current knowledge of the binary population in the Galactic Centre is limited, close binary systems remain as a very promising possibility for the creation of cold clumps. A more detailed numerical model of this process is deferred to a forthcoming paper.

6 CONCLUSIONS

We have developed a simple and straightforward prescription to study clump formation through the NTSI mechanism in symmetric colliding wind systems. The input parameters are the mass-loss rate, wind terminal velocity and stellar separation. Radiatively efficient wind collisions are capable of creating cold gas clumps (10^4 K) in a wide range of masses, where the most massive ones are of the order of the Earth mass for strong outflows ($\dot{M} \sim 10^{-5}$ $M_\odot$ yr^{-1}), relatively slow wind terminal velocities (250–750 km s^{-1}) and short stellar separations (0.1–10 mpc or 20–2060 au). Nevertheless, the wide range of unstable wavelengths that are excited prevents us from predicting unequivocal clump masses, as shorter wavelength perturbations grow faster and might hinder the development of larger scale ones.

We also found that the possible clump masses depend strongly on the time-scale needed for the slab to collapse within the radiative wind regime. The most massive ones would be generated in systems where the shocked gas does not cool instantaneously, i.e. systems with χ approaching unity. Studying that regime however is not straightforward as both radiative and adiabatic cooling are important.

Our results show that the formation of gas clumps with masses comparable to the G2 cloud is indeed possible in symmetric colliding winds. However, this scenario does not seem likely in the Galactic Centre given the currently known mass-losing star sample, as the required sub-mpc separations are very rarely achieved by them. We also discussed clump formation in asymmetric encounters, finding that the massive and slow outflow of IRS 33E could create clumps if confined by a powerful wind of another star. Similarly, the collision of winds from IRS 13E2 and 13E4 could also generate a cold slab unstable to the NTSI. These stars have similar orbits and spend a significant time at short separations, which could explain the presence of many dusty clumps in their vicinity (see Fritz et al. 2010). However, they orbit Sgr A* in the opposite sense as G2, making this pair an unlikely origin for this particular cloud. A promising possibility is that clumps are produced in close binaries, of which three are currently know. Still, better observational data are required to constrain the wind properties of both components of each binary. The IRS 16SW binary is of particular interest, as its orbit coincides with G2's at apocentre.

In conclusion, given our current analysis and the available stellar wind data, the formation of G2-like clouds in the Galactic Centre appears as a possible but not very common event. We defer more concrete results to a future study using 2D and 3D numerical modelling. This is required to treat systems with unequal stellar winds, with $\chi \sim 1$, or for winds that collide before reaching their terminal velocity, such as compact binaries. Numerical models are also required to follow the growth of different unstable wavelengths and obtain a clump mass function.

ACKNOWLEDGEMENTS

We thank the anonymous referee for very useful comments. We also thank Cristian Hernández for double checking some of the calculations. Part of this work was carried out at MPE, which DC and JC thank for the warm hospitality. We acknowledge support from CONICYT–Chile through FONDECYT (1141175), Basal (PFB0609) and Anillo (ACT1101) grants. DC is supported by CONICYT–PCHA/Doctorado Nacional (2015–21151574). AB was supported by the Deutsche Forschungsgemeinschaft (DFG) priority programme 1573 (Physics of the Interstellar Medium) and by the DFG Cluster of Excellence 'Origin and Structure of the Universe'.

REFERENCES

Alexander T., 2005, Phys. Rep., 419, 65
Ballone A. et al., 2013, ApJ, 776, 13
Boloborodov A. M., Levin Y., Eisenhauer F., Genzel R., Paumard T., Gillessen S., Ott T., 2006, ApJ, 648, 405
Burkert A., Schartmann M., Alig C., Gillessen S., Genzel R., Fritz T. K., Eisenhauer F., 2012, ApJ, 750, 58
Cuadra J., Nayakshin S., Springel V., Di Matteo T., 2005, MNRAS, 360, L55
Cuadra J., Nayakshin S., Springel V., Di Matteo T, 2006, MNRAS, 366, 358
Cuadra J., Nayakshin S., Martins F., 2008, MNRAS, 383, 458
Cuadra J., Nayakshin S., Wang Q. D., 2015, MNRAS, 450, 277
De Colle F., Raga A. C., Contreras-Torres F. F., Toledo-Roy J. C., 2014, ApJ, 789, L33
Dgani R., Walder R., Nussbaumer H., 1993, A&A, 267, 155
Eckart A. et al., 2013, A&A, 551, A18
Fritz T. K. et al., 2010, ApJ, 721, 395
Genzel R., Eisenhauer F., Gillessen S., 2010, Rev. Mod. Phys., 82, 3121
Gillessen S. et al., 2012, Nature, 481, 51
Gillessen S. et al., 2013, ApJ, 763, 78
Guillochon J., Loeb A., MacLeod M., Ramirez-Ruiz E., 2014, ApJ, 786, L12
Hobbs A., Read J., Power C., Cole D., 2013, MNRAS, 434, 1849
Kee N. D., Owocki S., ud-Doula A., 2014, MNRAS, 438, 3557
Lamberts A., Fromang S., Dubus G., 2011, MNRAS, 418, 2618
Lebedev M. G., Myasnikov A. V., 1990, Fluid Dyn., 25, 629
Lützgendorf N. et al., 2015, preprint (arXiv:1501.07441)
McCourt M., O'Leary R. M., Madigan A.-M., Quataert E., 2015, MNRAS, 449, 2
Martins F. et al., 2006, ApJ, 649, L103
Martins F., Genzel R., Hillier D. J., Eisenhauer F., Paumard T., Gillessen S., Ott T., Trippe S., 2007, A&A, 468, 233
Murray-Clay R. A., Loeb A., 2012, Nat. Commun., 3, 1049
Paumard T. et al., 2006, ApJ, 643, 1011
Pfuhl O., Alexander T., Gillessen S., Martins F., Genzel R., Eisenhauer F., Fritz T. K., Ott T., 2014, ApJ, 782, 101
Pfuhl O. et al., 2015, ApJ, 798, 111
Phifer K. et al., 2013, ApJ, 773, L13
Pittard J. M., 2009, MNRAS, 396, 1743
Prodan S., Antonini F., Perets H. B., 2015, ApJ, 799, 118

Schartmann M., Burkert A., Alig C., Gillessen S., Genzel R., Eisenhauer F., Fritz T., 2012, ApJ, 755, 155
Scoville N., Burkert A., 2013, ApJ, 768, 108
Stevens I. R., Blondin J. M., Pollock A. M., 1992, ApJ, 386, 265
Sutherland R. S., Dopita M. A., 1993, ApJS, 88, 253
van Marle A. J., Smith N., Owocki S. P., van Veelen B., 2010, MNRAS, 407, 2305
Vishniac E. T., 1983, ApJ, 274, 152
Vishniac E. T., 1994, ApJ, 428, 186
Witzel G. et al., 2014, ApJ, 796, 8
Yelda S., Ghez A. M., Lu J. R., Do T., Meyer L., Morris M. R., Matthews K., 2014, ApJ, 783, 131

This paper has been typeset from a TEX/LATEX file prepared by the author.